Time-resolved *operando* DRIFTS study of the moisture tolerance of small-pore SAPO-34 molecular sieves during CH_4/CO_2 separation

Marta Romero, Juan C. Navarro, Luis F. Bobadilla, María I. Domínguez, Svetlana Ivanova, Francisca Romero-Sarria, Miguel A. Centeno and José A. Odriozola*

Instituto de Ciencia de Materiales de Sevilla – Dpto. Química Inorgánica, Centro mixto CSIC – Universidad de Sevilla, Av. Américo Vespucio 49, 41092 Sevilla (Spain)

(*) Corresponding autor: bobadilla@icmse.csic.es (Luis F. Bobadilla)

Abstract

This study offers reliable information for understanding the effect of the presence of moisture during CO_2/CH_4 separation on small-pore SAPO-34 molecular sieves. Two SAPO-34 samples with different physicochemical properties (chemical composition, crystal size and textural properties) were prepared by hydrothermal synthesis using a unique template or mixing-templates, respectively. By means of a transient *operando* DRIFTS study switching adsorption/desorption cycles, it was proven that the presence of larger Si islands in the 8-membered ring cavities increases the hydrophobic character and enhances the moisture tolerance of the SAPO-34. This knowledge is fundamental for achieving the rational design of SAPO-34 membranes more efficient under realistic conditions.

Keywords: *SAPO-34; CO_2/CH_4 separation; moisture tolerance; operando DRIFTS*

1. Introduction

Climate change has been an active topic for both scientific and political debate during the last decades. International Panel on Climate Change (IPCC) predicts that, by the year 2100, the concentration of CO_2 in the atmosphere can achieve a value of 570 ppmv provoking an increase of the mean global temperature of 2 ºC and elevating the sea level above 38 m [1]. Currently, the perception of public opinion on global warming is becoming more generalized and exist a genuine concern in the society to reduce the CO_2 emissions [2, 3].

The utilization of technologies based on the transformation of residual biomass into energy such as the production of biogas is believed to be one of the best options to satisfy the high global energy demand and mitigate the CO_2 emissions [4]. Biogas is a promising renewable resource which is mostly comprised of methane (60%) and carbon dioxide (35–40%), and can be produced from a process known as biomass anaerobic digestion [5]. Biogas upgrading is required to separate the CO_2 from CH_4 and to obtain an enriched biomethane suitable for energetic uses as substitute of the natural gas. In this regard, several technologies such as absorption [6, 7] , cryogenic distillation [8, 9], membrane separation [10, 11] , and adsorption [12, 13] are commercially available for biogas upgrading. The separation of CO_2 without large energetic costs is highly desirable, and thus the utilization of membranes that preferentially permeate CO_2 at high selectivities can significantly reduce the costs of biogas purification [14]. In comparison to conventional polymeric membranes, materials based on microporous inorganic materials such a zeolites are preferably used for CO_2/CH_4 separation due to their superior thermal, mechanical and chemical strength as well as high pressure stability [15].

Zeolites are aluminosillicate crystalline solids with uniform-sized pores below 1 nm. Numerous studies have demonstrated the potential of zeolite-based materials as membranes for gas permeation and separation [16-18]. The zeolite membranes typically

prepared and used for gas separation can be distinguished into three categories: large-pore (Y-type, X-type, MOR, and beta), medium-pore (ZSM-5, ZSM-11, and FER), and small-pore (SAPO-34, A-type, SSZ-13, ALPO-18, and SSZ-13) [15, 19]. Meanwhile, the small-pore zeolites are typically preferred for separating selectively mixtures of CO_2 and methane due to a combination of differences in molecular diffusivity and competitive adsorption [20, 21]. SAPO-34 membranes have been potentially used for CO_2/CH_4 mixtures separation [21-27]. The SAPO-34 is a crystalline microporous silicoaluminophosphate with chabazite (CHA) framework structure which possesses a three dimensional system of 8-membered rings pores of 0.38 nm diameter [28]. This diameter is essentially the same as the kinetic diameter of methane (0.38 nm) but higher than CO_2 (0.33 nm), thereby CO_2 can diffuse towards the channels and adsorb on the pores.

From the viewpoint of industrial applications, the presence of impurities in the stream can negatively affect the performance of SAPO-34 membranes in the separation process. This effect is especially notable in presence of water, which even in very small quantities is strongly adsorbed in SAPO-34 and supress drastically the CO_2 uptake. Some studies have explored the effect of the presence of water in the CO_2/CH_4 separation. Poshusta et al. [29] found that the presence of water almost completely blocks the pores of the zeolite inhibiting the entrance of the other gases. In other work, Li et al. [30] studied the effect of a mixture of impurities composed by water, nitrogen, propane, butane, and ethylene on the CO_2/CH_4 separation over a SAPO-34 membrane supported on stainless steel. They found that after exposure to water and hydrocarbons in the feed, the permeance and selectivity of SAPO-34 membrane were both decreased although reversibly restored by thermal treatment. It is well known that by varying Si/Al ratio of zeolites is possible to fine-tune the hydrophobic/hydrophilic nature of the zeolite [31]. High-silica zeolites are typically more hydrophobic and resistant to the presence of moisture. Furthermore, zeolites with high silicon content are found to be less defective

and thus the gases transport inhibition associated to structural defects are reduced. Recently, Lee et al. [32] investigated the role of hydrophobicity and defect structure on rich-siliceous chabazite-type zeolites membranes and they found that the CH_4/CO_2 separation factor is enhanced in presence of water vapour due to the defects are blocked by physisorbed water molecules.

Although several works have been reported analysing the effect of the presence of moisture and other impurities on CH_4/CO_2 separation over SAPO-34 membranes, up to now limited studies have been focused on investigating simultaneously the surface properties of SAPO-34 and its functionalities under operation conditions. Wuttke et al. [33] reported for the first time an infrared spectroscopic characterisation study during a separation process by using the *operando* methodology. The Latin term *operando* is referred to the spectroscopic characterization of the material when is "working" and simultaneously the performance is analysed. Hence, *operando* measurements allow to establish directly a structure-performance relationship and can guide the rational design of more efficient materials. Diffuse reflectance infrared Fourier transform spectroscopy (DRIFTS) is a very sensitive technique to get insight into the surface species involved in a chemical process under working conditions. This report concerns the use of DRIFTS for monitoring the dynamic surface structure of SAPO-34 during CO_2/CH_4 separation and how can be affected the surface by the presence of trace amounts of moisture. With the aim of understanding the origin of moisture tolerance, two SAPO-34 molecular sieves with different crystal size and Si/Al molar ratio were investigated.

2. Experimental section

2.1. Chemicals

Aluminum isopropoxide (Sigma-Aldrich, 98%), colloidal silica (Ludox AS-40, 40 wt.%, Sigma-Aldrich) and orthophosphoric acid (Sigma-Aldrich, 85%) were used as precursors of the framework elements. The tetraethyl ammonium hydroxide (TEAOH, Sigma-

Aldrich, 35 wt.% aqueous solution) and dipropylamine (DPA, Sigma-Aldrich, 99%) were used as structure-directing agent for SAPO-34 synthesis. All chemicals purchased were used as received without any further purification.

2.2. Preparation of SAPO-34 molecular sieves

Two SAPO-34 molecular sieves denoted as S1 and S2, respectively, were prepared via hydrothermal synthesis using two different organic templates at 200 ºC as described Bai et al. [34]. The template agent used for S1 sample was TEAOH whereas a combination of TEAOH and DPA was used as mixed templates for S2 sample. The seed gel molar composition for each sample is given in Table 1.

In a typical synthesis procedure, S1 sample was prepared using TEAOH as template agent. First, a seed precursor solution was prepared by stirring a mixture of aluminum isoproxide, TEAOH, and deionized water for 2 h to achieve a homogenous solution. Then a colloidal silica suspension was added and the resulting solution was kept in agitation for another 2 h. Finally, an aqueous solution of ortophosphoric acid was added slowly and the solution was stirred for 3 days at room temperature to form a gel with a molar composition of 1.0 Al_2O_3 : 2.0 P_2O_5: 0.6 SiO_2:4.0 TEAOH : 75 H_2O. This gel was poured in a Teflon autoclave and the hydrothermal treatment was performed at 200 ºC for 24 h. The obtained seeds crystals were recovered by centrifugation, washed three times with deionized water, dried overnight, and then calcined in air at 550 ºC for 6 h with a heating rate of 1 ºC min^{-1} for removing the template.

The synthesis of S2 sample was carried out using a combination of two templates (TEAOH and DPA) as structure-directing agent. The gel molar composition of this SAPO-34 was 1.0 Al_2O_3 : 1.0 P_2O_5 : 0.3 SiO_2 : 1.0 TEAOH : 1.6 DPA : 77 H_2O. In this procedure, an aqueous solution of ortophosphoric acid and aluminium isopropoxide was initially kept in agitation for 3 h. Afterwards, Ludox colloidal silica was added and stirred for other 3 h. Then, TEAOH (35 wt% aqueous solution) and DPA were added and the resulting

solution was stirred for six days at room temperature. From here, the procedure used to obtain the S2 sample was identical to that used for S1 sample.

2.3. Materials characterization

The chemical composition was analysed by X-ray fluorescence (XRF) spectrometry on an AXIOS PANalytical spectrometer with Rh tube as source of radiation. The measurements were carried out onto pressed pellets (sample including 6 wt.% of wax). The textural properties of the samples were determined by nitrogen adsorption-desorption measurements at 77 K using a Micromeritics Tristar II instrument. Prior to each measurement, the zeolites were degassed at 400 °C for 2 h in vacuum. The specific surface area (S_{BET}), micropore surface area (S_{micro}) and micropore pore volume (V_{micro}) for each sample were estimated by the BET (Brunauer–Emmett–Teller) equation and t-plot method, respectively. X-ray powder diffraction (XRD) patterns were recorded on an X'Pert Pro Powder Diffractometer by PANalytical employing Cu-*K*α radiation (λ = 0.154 nm) at 30 mA and 40 kV. Data were collected in the range of 5° ≤ 2θ ≤ 40° with a step size of 0.05° every 240 s. The obtained patterns were identified using as reference the JCPDS (Joint Committee of Powder Diffraction Standards) index. The surface morphology of the materials was analysed by scanning electron microscopy (SEM) on a JEOL 5400 microscope operating at 20 kV. The samples were previously coated with a thin layer of gold to prevent charging problems. CO_2 adsorption isotherms were tested at 25 ºC on an ASAP 2420 model instrument from Micromeritics. Prior to adsorption isotherm measurement, the samples were pretreated at 450 ºC for 2 h in vacuum for removing the adsorbed species.

2.4. *Operando* DRIFTS experiments

Operando DRIFTS measurements were performed in a high-temperature environmental reaction chamber supported in a Praying Mantis (Harrick) optical system with ZnSe windows. The spectra were recorded with an average of 64 scans per

spectrum at 4 cm^{-1} of resolution in a Thermo Nicolet iS50 FTIR spectrometer equipped with a liquid nitrogen cooled MCT detector. Prior to the measurements, the sample was *in situ* pretreated at 550 ºC during 1 h under a flow rate of 100 mL min^{-1} of argon for removing the adsorbed water. For the time-resolved experiments of CO_2/CH_4 separation, a stream of 100 mL min^{-1} of 3.6% CO_2 and 5.4% CH_4 balanced in Ar (molar ratio of CH_4/CO_2 = 1.5) and a flow of 100 mL min^{-1} of Ar both including traces of water were switched with a 4-way valve and introduced into the IR cell every 300 s under isothermal conditions at 30 ºC. A background spectrum was collected without sample using an aluminium mirror, and all spectra of the adsorbed species on the solid surface were obtained by subtracting the spectrum of the sample after pretreatment.

3. Results and discussion

3.1. Chemical composition, structural analysis and morphology

The molar composition of the starting synthesis gel used to prepare both samples and the final crystal composition determined by XRF on both SAPO-34 powders are listed in Table 1. As can be observed, the Si/Al ratios of the crystal powders obtained are slightly higher than the initial gel mixture in each case. This indicates that the molar percent of silicon in both final SAPO-34 was higher than that of the starting gel and consequently Si is incorporated into the framework by substitution of Al and/or P atoms. It has been established that the incorporation of Si into the $AlPO_4$ framework can proceeds by two different substitution mechanisms [35, 36]: (i) the substitution of phosphorous atoms by atoms of silicon to form Si(4Al) entities which are known as “isolated Si”, and (ii) the double substitution of neighbouring Al and P by two silicon atoms to Si(*n*Al) with *n* = 0 – 3 entities designated as “Si islands”. The two substitution mechanisms are influenced by the synthesis conditions and the simultaneous occurrence of both mechanisms can also takes place resulting the presence of different silicon environments in which Si(*n*Al) structures coexist at the border of silicon islands [37]. Sastre et al. [36] used the topological density concept (TDC), which is related to the number of isolated silicon

atoms that can be found in a SAPO-34, to determine the maximum Si content at which all the silicon atoms can be present into the framework as isolated Si entities. Accordingly, this value is given by the ratio Si/(Si + Al + P) = 0.108 and represent the topological limit above which some non-isolated SiO_4 entities or Si islands will be formed in the structure. Consequently, a large amount of silicon islands are formed when Si content is high, whereas only isolated Si domains exists when Si content is low [38]. As can be observed in Table 1, these values are higher than 0.108 in both samples suggesting the presence of Si islands. Comparing both samples, it should be noted that S2 sample present a ratio only slightly above than 0.108 and although the presence of Si islands is unavoidable the number of isolated silicon atoms will be considerably superior in this sample. The relative proportion between Si islands and isolated Si affects directly to the variation in acidic properties of the resulting materials. Sastre et al. [36] established a direct correlation between acidity and Si island size, suggesting that the number of stronger acid sites is directly related to the concentration of Si islands and that the strength of the acid sites generated at the border of the Si islands will increase with Si island size. Nonetheless, it must be remarked that although the number of strong acid sites increases with the concentration of Si islands, the Si incorporation also increases the Si/Al ratio and, consequently, diminishes the total acidity of SAPO-34. Therefore, it can be expected that S1 sample present lower total acidity but higher number of strong acid sites associated to Si islands than S2 sample.

The crystal structure and morphology of both SAPO-34 molecular sieves were analysed by XRD and SEM, respectively. Figure 1a shows the XRD patterns of the prepared powder materials and clearly demonstrates the formation of the typical chabazite (CHA) structure with high degree of crystallinity in both samples. It should be mentioned that any additional peak associated to impurities phases was detected. The average crystallite sizes (nm) were calculated by Scherrer equation using the full width of diffraction peak at half maximum intensity (peak at $2\theta = 9.58$ º). As shown Table 1, it

is noteworthy that the S2 sample present an average crystalline size larger than S1 sample. Figure 1b shows SEM micrographs of the S1 and S2 samples. Both resulting materials exhibit a similar morphology based on cubic-like aggregated crystals. As illustrated SEM images, it is obvious that the crystal size of S2 sample became bigger than that of S1 sample in agreement with the values determined by using the Scherrer equation. It is well stablished that the crystal size of a SAPO-34 molecular sieve may change with the use of different templates. For instance, Nishiyama et al. [39] reported that the crystallization processes in the synthesis of SAPO-34 depend on the sort of template used, because both the nucleation and crystal-growth rates depend significantly on the interaction between the template and the inorganic species in the medium. Hence, the presence of a mixture of TEAOH and DPA in the synthesis of S2 SAPO-34 leads to larger crystals evidencing that the crystal growth step is intimately dependent on the type of template.

3.2. Textural properties and CO_2 adsorption capacity

Figure 2 shows the N_2 adsorption-desorption isotherms at 77 K for both SAPO-34 samples, S1 and S2. According to the IUPAC classification [40], the two zeolites exhibit typical type I isotherms, which is indicative of microporous solids. Data of surface area S_{BET}, micropore surface area and micropore volume estimated from the isotherms are included in Table 2. It is evident that the S1 SAPO-34 possess higher values of S_{BET}, micropore surface area and micropore volume than S2 sample. These differences are expected in base to the smaller crystal size of S1 sample.

Figure 3 provides the CO_2 adsorption isotherms at 25 ºC for S1 and S2 samples, respectively. In both samples, the adsorption isotherms satisfied the dual-site Langmuir-Freundlich model implying that the CO_2 adsorption corresponds to exothermic physisorption [41]. As shown Fig. 3 inlet, a gradual increase is observed in the low-pressure adsorption isotherm region for S2 SAPO-34 whereas an abrupt change in the slope is evidenced for S1 SAPO-34. This slight variation on the adsorption behaviour at

low pressures can become significant and suggests the presence of different adsorption sites which could be directly related to the relative amount of Si islands and isolated Si domains in the SAPO-34 framework. We speculate that the major concentration of Si islands predicted for S1 SAPO-34 could be the reason which explains the differences observed in the low-pressure CO_2 adsorption region. As we mentioned above, the possible formation of larger silicon islands in S1 SAPO-34 induces the creation of additional strong acidic adsorption sites at the edges of Si islands in which the interaction with CO_2 is weaker than that of the acid sites created by the isolated Si atoms. On the other hand, Table 2 shows that the value of CO_2 uptake in S1 sample is higher than the one observed for S2 sample, and it is likely due to the smaller crystal size of S1 sample.

3.2. Time-resolved *operando* DRIFTS study

With the aim of understanding the effect of the physicochemical properties in the origin of the moisture tolerance, an *operando* DRIFT spectroscopic study was performed over both SAPO-34 materials.

3.2.1 Dehydration pretreatment

Firstly, the samples were heated at 550 ºC for 1 h under argon flow to remove the adsorbed water on the surface and completely dehydrate the zeolite. The evolution of the IR spectra during the pretreatment of both SAPO-34 samples are shown in Figures 4a and 4b, respectively. As can be observed, both S1 and S2 samples are highly hydrated before pretreatment and the spectra are dominated by a very broad absorption band centered at 3400 cm^{-1} that can be assigned to the hydroxyl stretching modes of both physisorbed water molecules and hydroxyl groups interacting by hydrogen bonds [42]. On the counterpart, the band observed at 1630 cm^{-1} is associated to the bending vibration mode (δ_{HOH}) characteristic of physisorbed water in the SAPO-34 cages [42]. Furthermore, an additional broad band is also present at higher wavenumbers (5248 cm^{-1}) and this feature can be assigned to the $(v + \delta)_{HOH}$ combination mode characteristic of

molecular water adsorbed [43]. During the dehydration pretreatment, it is noticeable in both samples the disappearance of the broad band at 3400 cm^{-1} and the band at 1630 cm^{-1} both associated to adsorbed water, and at the same time the appearance of well-defined bands in the 3800 – 3600 cm^{-1} range which are typical of free hydroxyl species. Moreover, it can be noted the appearance of a broad band centered at 2205 cm^{-1} which can be ascribed to overtone and combination vibration modes associated to PO_4 units [44]. Additionally, the combination mode of molecular water at 5248 cm^{-1} also vanished whereas simultaneously new redshifted bands (4670 and 4648 cm^{-1}) appeared forming an evident isosbestic point. These new features correspond to the combination bands of stretching and bending vibrations $(\nu + \delta)_{OH}$ of surface hydroxyl groups [45].

3.2.2 Nature and IR assignment of hydroxyl groups

The complexity of the bands associated to hydroxyl groups in the IR spectra after pretreatment requires a more detailed discussion to analyse the nature of the OH species. Figure 5a shows the IR spectra in the region of the fundamental stretching vibrations associated to hydroxyl groups (3000 – 4000 cm^{-1}) in both SAPO-34 samples after pretreatment. The bands at 3630 and 3603 cm^{-1} are the high (type I) and low (type II) frequency hydroxyl stretching vibrations, respectively, associated to the Si(OH)Al Brønsted acid sites located at different crystallographic positions on SAPO-34 [46]. Both types of acid sites exhibited essentially similar acidic properties but differed in their localization inside the cavity. It can be assumed that the hydroxyl groups at 3630 cm^{-1} (type I) are likely localized in the 8-membered rings ellipsoidal cavities whereas the ones at 3599 cm^{-1} (type II) are located in the 6-membered rings hexagonal prisms cavities forming a hydrogen bonds with adjacent oxygen atoms of the framework [47]. Meanwhile, the low-intensity features appearing at 3673, 3745 and 3775 cm^{-1} can be ascribed to phosphorus hydroxyl (P-OH), terminal silanol (Si-OH) and aluminium hydroxyl (Al-OH) groups, respectively, which likely are located on the most external surface of the zeolite [47, 48]. Consequently, these species will be more abundant in S1

sample characterized by a small crystallite size and higher specific surface area than S2 sample.

The evaluation of spectral range expanded to higher frequencies comprised between 4000 and 8000 cm^{-1} in the near-infrared region (NIR) allows one to obtain valuable information on the combination of stretching (ν) plus bending (δ) vibrations modes and the overtones associated to stretching vibrations (ν_{0-n}) of surface hydroxyl species. The combination of fundamental stretching (3500 – 3800 cm^{-1}) and bending modes (600 – 1640 cm^{-1}) of structural hydroxyl groups are very useful to estimate indirectly the bending modes of hydroxyl groups which appear in the 700 – 1100 cm^{-1} range [45]. Typically, the deformation modes cannot be observed directly in the IR spectrum because they are overlapped by Al-O and Si-O framework vibrations [49]. Figures 5b and 5c show the region of the combination modes of stretching plus in-plane bending vibrations (ν + δ) and of the first overtones of the stretching vibrations of hydroxyl groups for both SAPO-34 samples. The assignment of the bands observed in the near infrared region and the correspondence with the features of the fundamental range are given in Table 3. The deformation vibrational modes (δ) were estimated by subtraction of the stretching fundamental mode (ν) from the combination band (ν + δ). It is well known that generally the wavenumber of the combination band is lower than the sum of the two fundamental modes due to the interaction between both vibrations. Nevertheless, it has been found that the coefficient of the interaction between stretching and bending vibrations for different types of surface hydroxyls in SiO_2 and H-form zeolites is close to zero [49]. Thus, we can be assured that the values of bending modes estimated for SAPO-34 are accurate. On the other hand, the assignment of the overtones is made on the basis of a general rule which establish that the wavenumber of the first overtone appear always at a wavenumber lower than twofold the fundamental stretching mode due to the anharmonicity factor [45, 50]. As can be observed in Fig. 5c, only the bands at 7044 and 7099 cm^{-1} associated to the first overtone of bridged hydroxyls Si(OH)Al were

distinguished although with poor resolution, whereas the bands at 7220, 7320 and 7430 cm^{-1}corresponding to the first overtone of P-OH, Si-OH and Al-OH species, respectively, were hardly observed. This arises because the band intensities in the overtones region are generally by one to two orders of magnitude lower than those of fundamental region.

The detailed analysis of the combination bands can provide more clear information than the fundamental region on the nature and the structural environment of the hydroxyl groups. Figure 5b shows the results fitted with Gaussians curves in the region of combination bands, in which two different bands at 4670 and 4642 cm^{-1} can be clearly distinguished. These two bands are assigned to the combination bands $(\nu + \delta)_{OH}$ of bridged Si(OH)Al species located on in the ellipsoidal cavities (type I - 4670 cm^{-1}) and hexagonal prisms (type II - 4642 cm^{-1}) of the chabazite (CHA) framework in agreement with the mentioned above. This approach enables to estimate the fraction of the two different Brønsted acid sites in both S1 and S2 SAPO-34 samples. The relative fraction of $OH_{type\ I}$ and $OH_{type\ II}$ in both SAPO-34 materials was 2.069 for S2 sample and 1.410 for S1 sample. This suggest that the fraction of Brønsted acid sites located in the 8-membered ring cavities is significantly more pronounced in S2 SAPO-34 sample as compared with S1 SAPO-34 sample. Notice that the acidic properties of the bridged hydroxyl groups in SAPO-34 depend on the environment of the Si(OH)Al fragment. Moreover, in agreement with the hypothesis discussed above and depending on the amount of silicon incorporated into the framework, strong Brønsted acid sites are formed at the borders of silicon islands. The next part of this study concerns the analysis of the different acid sites present in each SAPO-34 sample upon the dehydration pretreatment in order to elucidate the effect of moisture presence during the CO_2/CH_4 separation process.

3.2.3 Transient study of CO_2/CH_4 separation performance

In order to fully compare the differences between SAPO-34 samples and gain more insight into of the hydroxyl groups interacting with the encaged species in the cavities of

SAPO-34 crystals during CO_2/CH_4 separation in presence of moisture, we have performed an *operando* transient DRIFT spectroscopic study to uncover the chemical nature of the species involved in the process.

Figure 6 illustrates the evolution of a series of IR spectra collected on both SAPO-34 samples at 30 ºC during alternate switching between pure argon and CO_2/CH_4/Ar (CH_4/CO_2 = 1.5) feeds both containing traces of water. As can be seen, the dynamics evolution of infrared spectra is shown such in a 3D representation (Fig. 6a and c) as in the 2D mapping (Fig. 6b and d) for both samples. During introduction of the CO_2/CH_4/Ar feed are clearly distinguished the IR bands attributed to CO_2 and CH_4 gas as well as the presence of a broad band centered at 3500 cm^{-1} which is associated to CO_2 weakly interacting with the hydroxyl groups [51]. It can be observed that upon switching from CO_2/CH_4/Ar to pure argon these features completely disappeared on both samples. Nevertheless, it is noteworthy that after several adsorption/desorption cycles appeared two bands at 2950 and 2450 cm^{-1} which progressively increasing the intensity. These two features correspond to the A and B components of the so called “ABC triplet” which is due to a strong interaction by hydrogen bonds involving the bridged hydroxyls and the water molecules [52]. The nature of this triplet has been extensively studied and can be ascribed to the Fermi resonance of the hydroxyl stretching mode (strongly shifted to lower frequencies) coupled with the first overtones of the in-plane and out-of-plane bending modes of the bridging hydroxyls, respectively [42, 52, 53]. The Fermi resonance takes place between two very close vibrational modes with the adequate symmetry. Apart from these two A-B bands, other three features at 3676, 3650 and 3567 cm-1 also remained during the adsorption/desorption cycles. These bands are also ascribed to the interaction of water molecules with structural hydroxyls at low water coverages [42]. It is particularly interesting to note that the presence of these latter bands and the formation of the A-B components occurs earliest in the S2 sample than S1. As will be further

discussed, this fact can be related to the different environment of the Si(OH)Al fragments and the silicon introduced into the framework in both SAPO-34 samples.

In some zeolites, the adsorption of water can induce the abstraction of the proton from Brønsted acid sites forming hydronium ions (H_3O^+), but this conception has been discarded by several authors through infrared and computational studies because neutral species are more stable than protonated species [42, 54]. Nevertheless, Vener et al. [55] predicted by density functional theory (DFT) calculations that the protonation state is found when the number of water molecules loaded per acid sites increase from 1 to 4 but single water molecules are not protonated. By contrast, Smith et al. [56] reported that both species, hydronium ions or merely water hydrogen-bonded to acid sites, are present inside the H-SAPO-34 channels. In fact, they demonstrated that H_3O^+ ions can be typically found in the eight-ring cavities of the zeolite and water hydrogen-bonded to acid sites are found on the six-membered rings. In our case of study, the developing of the A-B components with identical intensities suggest that water molecules interact with the Brønsted acid sites likely through hydrogen-bonds of medium strength without formation of protonated species. If very strong H-bonds were involved in the formation of $H^+(H_2O)$ clusters *via* abstraction of proton, it would be expected the formation of less prominent A- B components and a very broad C component [42, 57].

In order to examine in more detail the nature of the species involved in the process, Figure 7 includes the representative infrared spectra collected during the first cycle of adsorption/desorption in both samples. During the adsorption period, a new broad band around 3500 cm^{-1} accompanied by the characteristic combination modes ($v_3 + 2v_2$) and ($v_3 + v_1$) indicates the physical adsorption of CO_2 [51]. Upon desorption with pure Ar, these features were fully disappeared suggesting that CO_2 molecules only interacted very weakly with the hydroxyl groups. Although these observations are common in both SAPO-34 samples, significant differences are noticeable in the bands associated to fundamental stretching vibrations of hydroxyls in each case. The most distinctive

changes are related to the formation of three new bands at 3676, 3650 and 3567 cm^{-1} at the same time which decline the bands assigned to bridged hydroxyls (3630 and 3599 cm^{-1}). In agreement with Bordiga et al. [42], we speculate that these bands are associated to v_{OH} stretching modes of slightly perturbed H_2O molecules interacting with the bridged hydroxyl sites and they are typically observed at low coverages of water. It is reasonable to assume that the bands at 3676 and 3650 cm^{-1} are associated to the interaction of water molecules with the bridging hydroxyls located on the eight-membered rings (3630 cm^{-1}) and six-membered rings (3599 cm^{-1}), respectively. This assumption is in agreement with the attribution reported by Smith et al. [56]. Meanwhile, the band at 3567 cm^{-1} could be ascribed to the stretching mode of hydroxyls of H_2O molecules forming a single hydrogen bond with the adjacent oxygen atom of the framework in the six-membered cavities [58]. In Fig. 7 is clearly evidenced that the presence of these bands is minor in S1 SAPO-34 sample than in S2 sample pointing out that S1 is more tolerant to moisture than S2. The main reason for explaining this observation could be ascribed to the larger crystal size of S2 sample, in which more Si(OH)Al fragments are exposed to be attacked by water molecules. Moreover, the interaction of water with SAPO-34 depends on the distribution of silicon atoms into the framework and different studies pointing to the higher stability of SAPO-34 materials incorporating silicon islands in comparison to SAPO-34 with isolated Si atoms [59]. Thus, the major presence of Si islands in S1 SAPO-34 is other of the main reasons to explain the detrimental effect on the water adsorption properties of this sample.

Figure 8a provides a sketch of the chabazite (CHA) structure with space group R-3m and Figure 8b includes a schematic representation of the corresponding vibration modes associated to the interaction of water molecules with the Brønsted acid sites in SAPO-34. It is noteworthy to mention that as the pore size of SAPO-34 is determined by the diameter of the eight-membered rings (3.8 Å) only the molecules with a smaller kinetic diameter will be accessible to the structural hydroxyl groups of SAPO-34. Therefore, only

H_2O (2.65 Å) and CO_2 (3.3 Å) molecules can penetrate into the cavities of SAPO-34 while that methane (3.8 Å) molecules only will be perturbed by those hydroxyl groups which are located on the external surface of the crystallites. Furthermore, due to their small kinetic diameter, water molecules will be able to diffuse through the both 8-membered and 6-membered ring cavities. As shown Fig. 8c, the chabazite (CHA) topology involves four geometrically differently positions for Brønsted acid sites depending on to which framework oxygen atom the proton is attached. The usual nomenclature designates these four different oxygen sites as O1, O2, O3 and O4, respectively. The protons attached to O3 are not exposed to the eight-membered ring and consequently are distinctive from those attached to O1, O2, and O4 framework positions. Accordingly, Bordiga et al. [57] reported that the three protons attached to O1, O2 and O4 positions are all located on the 8-membered rings and they are represented by the fundamental stretching mode at 3630 cm^{-1}. In contrast, the protons attached to O3 sites are isolated inside of the *d6r* cages and are associated to the lower wavenumber of ν_{OH} (3599 cm^{-1}). This interpretation is supported by our experimental data and, as shown Fig. 7, it is obvious in both SAPO-34 samples that during adsorption of water molecules the band at 3630 cm^{-1} decays more rapidly than the band at 3599 cm^{-1}, revealing that the hydroxyls located on the great cavities are more accessible than the hydroxyls located inside of the *d6R* cages. Despite this, it is essential to know that by means of theoretical calculations have been demonstrated that exist energetic differences between the four oxygen sites and a fine analysis would not be limited exclusively to two sites [55, 60]. However, the energetic differences existing between O1, O2 and O4 are minor and our approach can be considered valid for explaining the experimental data.

In order to assess the evolution of the most relevant species involved during the cycles of adsorption/desorption over both SAPO-34 samples, Figure 9 displays the evolution of the IR peak heights plotted against time-on-stream. As can be observed, the

time evolution of physisorbed CO_2 (3500 cm^{-1}), adsorbed water at low coverages (3676 cm^{-1}) and molecular water occluded in the cavities (5248 cm^{-1}) present important differences. Here it becomes evident that the efficiency of CO_2 adsorption in S2 SAPO-34 is minor and decreases more rapidly than that of S1 sample. The evolution of the peak at 3676 cm^{-1} reveals that in S2 sample all the Brønsted acid sites were saturated with molecules of water whereas in S1 SAPO-34 the saturation was not reached. Consequently, the S2 SAPO-34 sample retains high surface coverage of water which occlud rapidly the cavities avoiding that CO_2 molecules pass through the channels. As was claimed above, the amount of adsorbed water depends on the amount of silicon introduced into the framework, which at the same time also determines the chemical composition of the environment of the Si(OH)Al fragments. The S1 sample is characterized by a minor concentration of Si(OH)Al acid sites in the 8-membered ring cavities and contains major amount of Si islands incorporated into the framework. It is expected that the presence of Si-rich regions favours the hydrophobicity of the material and, consequently, enhances the moisture tolerance.

In summary, we have monitored the evolution of the SAPO-34 surface to understand as the adsorption sites are blocked by physisorbed water molecules and we can conclude that an increase of the hydrophobicity by incorporating more Si into the framework is desirable for using SAPO-34 as membranes in realistic stream conditions containing water-vapor. This approach is very useful to achieve a rational design of materials which can be applied as membranes in large-scale separation processes.

4. Conclusions

In the present article, we have performed an *operando* DRIFT spectroscopic study to provide evidences on the effect of the chemical composition and the crystal size of SAPO-34 materials in the moisture tolerance during CO_2/CH_4 separation processes. It was found that the presence of larger silicon island in the 8-membered ring cavities increases the hydrophobicity of the SAPO-34 material and enhances the efficiency of

CO_2/CH_4 separation. Furthermore, these results provide new found potential for the use of SAPO-34 molecular sieves as membranes in the CO_2/CH_4 separation processes, which is often neglected as an industrially relevant material due to its low water tolerance.

Acknowledgments

Financial support for this work has been obtained from the Spanish Ministerio de Ciencia, Innovación y Universidades co-financed by FEDER funds from the European Union (RTI2018-096294-B-C33). Moreover, Luis F. Bobadilla thanks the contracts of Spanish Government financed in part by the European Regional Development Fund through the “Juan de la Cierva incorporación” program (IJCI-2015-26348).

References

[1] H. Yang, Z. Xu, M. Fan, R. Gupta, R.B. Slimane, A.E. Bland, I. Wright, Progress in carbon dioxide separation and capture: A review, J. Environ. Sci. 20 (2008) 14-27.

[2] A.T. Abeles, L.C. Howe, J.A. Krosnick, B. MacInnis, Perception of public opinion on global warming and the role of opinion deviance, J. Environ. Psychol. 63 (2019) 118-129.

[3] R.M. Cuéllar-Franca, A. Azapagic, Carbon capture, storage and utilisation technologies: A critical analysis and comparison of their life cycle environmental impacts, J. CO2 Util. 9 (2015) 82-102.

[4] M. Khalil, M.A. Berawi, R. Heryanto, A. Rizalie, Waste to energy technology: The potential of sustainable biogas production from animal waste in Indonesia, Renew. Sustain. Energy Rev. 105 (2019) 323-331.

[5] P. Abdeshahian, J.S. Lim, W.S. Ho, H. Hashim, C.T. Lee, Potential of biogas production from farm animal waste in Malaysia, Renew. Sustain. Energy Rev. 60 (2016) 714-723.

[6] S. Simonato, J. Möllmer, M. Lange, R. Gläser, R. Staudt, C. Feldmann, Selective separation of CO_2–CH_4 mixed gases via magnesium aminoethylphosphonate nanoparticles, RSC Adv. 6 (2016) 12446-12452.

[7] W. Kamopas, A. Asanakham, T. Kiatsiriroat, Absorption of CO_2 in biogas with amine solution for biomethane enrichment, J. Eng. Technol. Sci. 48 (2016) 231-241.

[8] A.M. Yousef, W.M. El-Maghlany, Y.A. Eldrainy, A. Attia, Upgrading biogas to biomethane and liquid CO_2: A novel cryogenic process, Fuel 251 (2019) 611-628.

[9] Y. Tan, W. Nookuea, H. Li, E. Thorin, J. Yan, Cryogenic technology for biogas upgrading combined with carbon capture - a review of systems and property impacts, Energy Procedia 142 (2017) 3741-3746.

[10] D. Iarikov, S. Oyama, Review of CO_2/CH_4 separation membranes, Memb. Sci. Technol. 14 (2011) 91-115.

[11] Y. Zhang, J. Sunarso, S. Liu, R. Wang, Current status and development of membranes for CO_2/CH_4 separation: A review, Int. J. Greenh. Gas Con. 12 (2013) 84-107.

[12] Y.-S. Bae, K.L. Mulfort, H. Frost, P. Ryan, S. Punnathanam, L.J. Broadbelt, J.T. Hupp, R.Q. Snurr, Separation of CO_2 from CH_4 using mixed-ligand metal−organic frameworks, Langmuir 24 (2008) 8592-8598.

[13] S. Cavenati, C.A. Grande, A.E. Rodrigues, Separation of $CH_4/CO_2/N_2$ mixtures by layered pressure swing adsorption for upgrade of natural gas, Chem. Eng. Sci. 61 (2006) 3893-3906.

[14] S.R. Venna, M.A. Carreon, Highly permeable zeolite imidazolate framework-8 membranes for CO_2/CH_4 Separation, J. Am. Chem. Soc. 132 (2010) 76-78.

[15] S. Li, J.L. Falconer, R.D. Noble, SAPO-34 membranes for CO_2/CH_4 separation, J. Memb. Sci. 241 (2004) 121-135.

[16] Y. Li, H. Yi, X. Tang, F. Li, Q. Yuan, Adsorption separation of CO_2/CH_4 gas mixture on the commercial zeolites at atmospheric pressure, Chem. Eng. J. 229 (2013) 50-56.

[17] M. Mofarahi, F. Gholipour, Gas adsorption separation of CO_2/CH_4 system using zeolite 5A, Micropor. Mesopor. Mater. 200 (2014) 1-10.

[18] N. Rangnekar, N. Mittal, B. Elyassi, J. Caro, M. Tsapatsis, Zeolite membranes – a review and comparison with MOFs, Chem. Soc. Rev. 44 (2015) 7128-7154.

[19] N. Kosinov, J. Gascon, F. Kapteijn, E.J.M. Hensen, Recent developments in zeolite membranes for gas separation, J. Memb. Sci. 499 (2016) 65-79.

[20] N.O. Chisholm, H.H. Funke, R.D. Noble, J.L. Falconer, Effect of toluene adsorption on permeation through SAPO-34 membranes, J. Memb. Sci. 560 (2018) 108-114.

[21] S. Li, J.G. Martinek, J.L. Falconer, R.D. Noble, T.Q. Gardner, High-pressure CO_2/CH_4 separation using SAPO-34 membranes, Ind. Eng. Chem. Res. 44 (2005) 3220-3228.

[22] J.C. Poshusta, V.A. Tuan, E.A. Pape, R.D. Noble, J.L. Falconer, Separation of light gas mixtures using SAPO-34 membranes, AIChE J. 46 (2000) 779-789.

[23] H.H. Funke, M.Z. Chen, A.N. Prakash, J.L. Falconer, R.D. Noble, Separating molecules by size in SAPO-34 membranes, J. Memb. Sci. 456 (2014) 185-191.

[24] M.A. Carreon, S. Li, J.L. Falconer, R.D. Noble, Alumina-supported SAPO-34 membranes for CO_2/CH_4 separation, J. Am. Chem. Soc. 130 (2008) 5412-5413.

[25] S. Li, J.L. Falconer, R.D. Noble, Improved SAPO-34 membranes for CO_2/CH_4 separations, Adv. Mater. 18 (2006) 2601-2603.

[26] H. Shi, Organic template-free synthesis of SAPO-34 molecular sieve membranes for CO_2–CH_4 separation, RSC Adv. 5 (2015) 38330-38333.

[27] H. Shi, Synthesis of SAPO-34 zeolite membranes with the aid of crystal growth inhibitors for CO_2–CH_4 separation, New J. Chem. 38 (2014) 5276-5278.

[28] T. Wu, M.C. Diaz, Y. Zheng, R. Zhou, H.H. Funke, J.L. Falconer, R.D. Noble, Influence of propane on CO_2/CH_4 and N_2/CH_4 separations in CHA zeolite membranes, J. Memb. Sci. 473 (2015) 201-209.

[29] J.C. Poshusta, R.D. Noble, J.L. Falconer, Characterization of SAPO-34 membranes by water adsorption, J. Memb. Sci. 186 (2001) 25-40.

[30] S. Li, G. Alvarado, R.D. Noble, J.L. Falconer, Effects of impurities on CO_2/CH_4 separations through SAPO-34 membranes, J. Memb. Sci. 251 (2005) 59-66.

[31] N. Kosinov, C. Auffret, G.J. Borghuis, V.G.P. Sripathi, E.J.M. Hensen, Influence of the Si/Al ratio on the separation properties of SSZ-13 zeolite membranes, J. Memb. Sci. 484 (2015) 140-145.

[32] M. Lee, S. Hong, D. Kim, E. Kim, K. Lim, J.C. Jung, H. Richter, J.-H. Moon, N. Choi, J. Nam, J. Choi, Chabazite-type zeolite membranes for effective CO_2 separation: The role of hydrophobicity and defect structure, ACS Appl. Mater. Interfaces 11 (2019) 3946-3960.

[33] S. Wuttke, P. Bazin, A. Vimont, C. Serre, Y.-K. Seo, Y.K. Hwang, J.-S. Chang, G. Férey, M. Daturi, Discovering the active sites for C3 separation in MIL-100(Fe) by using operando IR spectroscopy, Chem. Eur. J. 18 (2012) 11959-11967.

[34] L. Bai, N. Chang, M. Li, Y. Wang, G. Nan, Y. Zhang, D. Hu, G. Zeng, W. Wei, Ultrafast synthesis of thin SAPO-34 zeolite membrane by oil-bath heating, Micropor. Mesopor. Mater. 241 (2017) 392-399.

[35] M. Ghavipour, A.S. Mehr, Y. Wang, R.M. Behbahani, S. Hajimirzaee, K. Bahrami, Investigating the mixing sequence and the Si content in SAPO-34 synthesis for selective conversion of methanol to light olefins using morpholine/TEAOH templates, RSC Adv. 6 (2016) 17583-17594.

[36] G. Sastre, D.W. Lewis, C.R.A. Catlow, Modeling of silicon substitution in SAPO-5 and SAPO-34 molecular sieves, J. Phys. Chem. B 101 (1997) 5249-5262.

[37] T. Álvaro-Muñoz, C. Márquez-Álvarez, E. Sastre, Use of different templates on SAPO-34 synthesis: Effect on the acidity and catalytic activity in the MTO reaction, Catal. Today 179 (2012) 27-34.

[38] W. Shen, X. Li, Y. Wei, P. Tian, F. Deng, X. Han, X. Bao, A study of the acidity of SAPO-34 by solid-state NMR spectroscopy, Micropor. Mesopor. Mater. 158 (2012) 19-25.

[39] N. Nishiyama, M. Kawaguchi, Y. Hirota, D. Van Vu, Y. Egashira, K. Ueyama, Size control of SAPO-34 crystals and their catalyst lifetime in the methanol-to-olefin reaction, Appl. Catal. A Gen. 362 (2009) 193-199.

[40] G. Leofanti, M. Padovan, G. Tozzola, B. Venturelli, Surface area and pore texture of catalysts, Catal. Today 41 (1998) 207-219.

[41] S.-M. Hong, E. Jang, A.D. Dysart, V.G. Pol, K.B. Lee, CO_2 capture in the sustainable wheat-derived activated microporous carbon compartments, Sci. Rep. 6 (2016) 34590.

[42] S. Bordiga, L. Regli, C. Lamberti, A. Zecchina, M. Bjørgen, K.P. Lillerud, FTIR adsorption studies of H_2O and CH_3OH in the isostructural H-SSZ-13 and H-SAPO-34: Formation of H-bonded adducts and protonated clusters, J. Phys. Chem. B 109 (2005) 7724-7732.

[43] W. Hanke, K. Möller, Near-infrared study of the dealumination and water desorption from zeolites, Zeolites 4 (1984) 244-250.

[44] S. Navarro-Jaén, F. Romero-Sarria, M.A. Centeno, O.H. Laguna, J.A. Odriozola, Phosphate-type supports for the design of WGS catalysts, Appl. Catal. B Environ. 244 (2019) 853-862.

[45] L.M. Kustov, V.Y. Borovkov, V.B. Kazansky, Spectra of hydroxyl groups in zeolites in the near-infrared region, J. Catal. 72 (1981) 149-159.

[46] Q. Qian, C. Vogt, M. Mokhtar, A.M. Asiri, S.A. Al-Thabaiti, S.N. Basahel, J. Ruiz-Martínez, B.M. Weckhuysen, Combined operando UV/Vis/IR spectroscopy reveals the role of methoxy and aromatic species during the methanol-to-olefins reaction over H-SAPO-34, ChemCatChem 6 (2014) 3396-3408.

[47] S.A. Zubkov, L.M. Kustov, V.B. Kazansky, I. Girnus, R. Fricke, Investigation of hydroxyl groups in crystalline silicoaluminophosphate SAPO-34 by diffuse reflectance infrared spectroscopy, J. Chem. Soc. Faraday Trans. 87 (1991) 897-900.

[48] G.V.A. Martins, G. Berlier, C. Bisio, S. Coluccia, H.O. Pastore, L. Marchese, Quantification of Brønsted acid sites in microporous catalysts by a combined FTIR and NH3-TPD study, J. Phys. Chem. C 112 (2008) 7193-7200.

[49] L.M. Kustov, New trends in IR-spectroscopic characterization of acid and basic sites in zeolites and oxide catalysts, Top. Catal. 4 (1997) 131-144.

[50] K. Hadjiivanov, Chapter Two - Identification and characterization of surface hydroxyl groups by infrared spectroscopy, in: F.C. Jentoft (Ed.) Advances in Catalysis, Academic Press, 2014, pp. 99-318.

[51] O. Cheung, Q. Liu, Z. Bacsik, N. Hedin, Silicoaluminophosphates as CO_2 sorbents, Micropor. Mesopor. Mater. 156 (2012) 90-96.

[52] M.F. Claydon, N. Sheppard, The nature of “A,B,C”-type infrared spectra of strongly hydrogen-bonded systems; pseudo-maxima in vibrational spectra, J. Chem. Soc. D (1969) 1431-1433.

[53] A. Gutiérrez-Alejandre, M.A. Larrubia, J. Ramirez, G. Busca, FT-IR evidence of the interaction of benzothiophene with the hydroxyl groups of H-MFI and H-MOR zeolites, Vib. Spectrosc. 41 (2006) 42-47.

[54] A.G. Pelmenschikov, R.A. van Santen, Water adsorption on zeolites: ab-initio interpretation of IR data, J. Phys. Chem. 97 (1993) 10678-10680.

[55] M.V. Vener, X. Rozanska, J. Sauer, Protonation of water clusters in the cavities of acidic zeolites: $(H_2O)n{\cdot}$H-chabazite, n = 1–4, Phys. Chem. Chem. Phys. 11 (2009) 1702-1712.

[56] L. Smith, A.K. Cheetham, R.E. Morris, L. Marchese, J.M. Thomas, P.A. Wright, J. Chen, On the nature of water bound to a solid acid catalyst, Science 271 (1996) 799.

[57] S. Bordiga, L. Regli, D. Cocina, C. Lamberti, M. Bjørgen, K.P. Lillerud, Assessing the acidity of high silica chabazite H−SSZ-13 by FTIR using CO as molecular probe: Comparison with H−SAPO-34, J. Phys. Chem. B 109 (2005) 2779-2784.

[58] P.-P. Knops-Gerrits, H. Toufar, X.-Y. Li, P. Grobet, R.A. Schoonheydt, P.A. Jacobs, W.A. Goddard, The structure of water in crystalline aluminophosphates: Isolated water and intermolecular clusters probed by Raman spectroscopy, NMR and structural modeling, J. Phys. Chem. A 104 (2000) 2525-2525.

[59] M. Fischer, Water adsorption in SAPO-34: elucidating the role of local heterogeneities and defects using dispersion-corrected DFT calculations, Phys. Chem. Chem. Phys. 17 (2015) 25260-25271.

[60] I. Halasz, B. Moden, A. Petushkov, J.-J. Liang, M. Agarwal, Delicate distinction between OH groups on proton-exchanged H-chabazite and H-SAPO-34 molecular sieves, J. Phys. Chem. C 119 (2015) 24046-24055.

Table 1. Chemical composition and average crystalline size of the SAPO-34 samples prepared

Sample (Template)	SiO_2:Al_2O_3:P_2O_5 Gel molar ratio	Crystal composition (*)	Si/Al molar ratio (Gel)	(Crystal)	Si/(Si + Al + P) molar ratio in crystal	Crystalline size / nm (**)
S1 (TEAOH)	0.3:0.5:1.0	$Si_{0.21}Al_{0.56}P_{0.23}O_2$	0.30	0.38	0.21	600
S2 (TEAOH/DPA)	0.3:1.0:1.0	$Si_{0.13}Al_{0.72}P_{0.15}O_2$	0.15	0.18	0.13	1000

(*) Analysed by X-ray fluorescence

(**) Estimated using the Scherrer equation

Table 2. Textural properties and CO_2 adsorption capacity for both SAPO-34 samples

Sample (Template)	Surface area (S_{BET}) $m^2\,g^{-1}$	t-plot micropore surface area / $m^2\,g^{-1}$	t-plot micropore volume / $cm^3\,g^{-1}$	CO_2 uptake mmol g^{-1}
S1 (TEAOH)	611	580	0.27	4.8
S2 (TEAOH/DPA)	568	525	0.25	4.3

Table 3. Assignment of the vibrational modes of hydroxyl groups

Nature of OH group	v / cm^{-1}	v + δ / cm^{-1}	δ / cm^{-1}	$v_{0\text{-}2\ overtones}$ / cm^{-1}
Si(OH)Al *type I*	3630	4670	1040 (*)	7090
Si(OH)Al *type II*	3599	4648	1049 (*)	7044
Si-OH	3745	4540 (weak)	795 (*)	7320 (weak)
P-OH	3673	not observed	-	7220 (weak)
Al-OH	3776	not observed	900-750 (**)	7430 (weak)
H_2O molecular	3300-3500	5000-5400	1630	6900-7400

(*) Calculated by subtraction from the combination band (v + δ)

(**) From ref. [49]

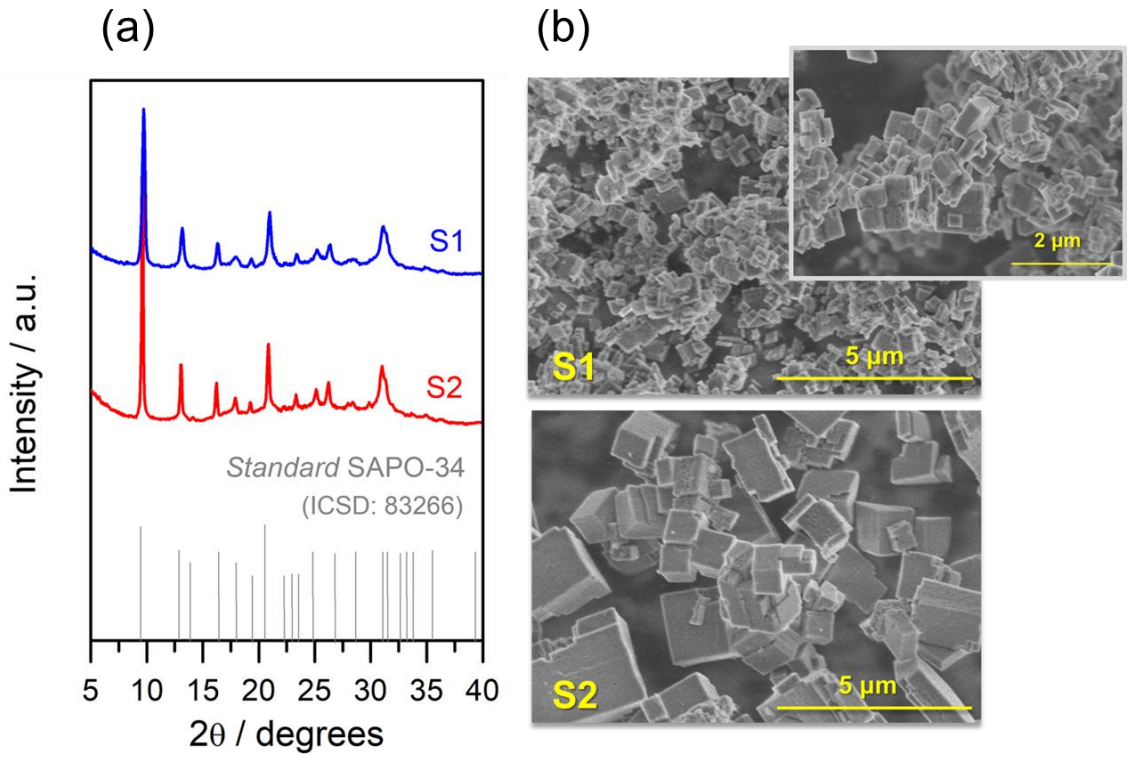

Figure 1. XRD patterns (a) and SEM micrographs (b) for both SAPO-34 samples

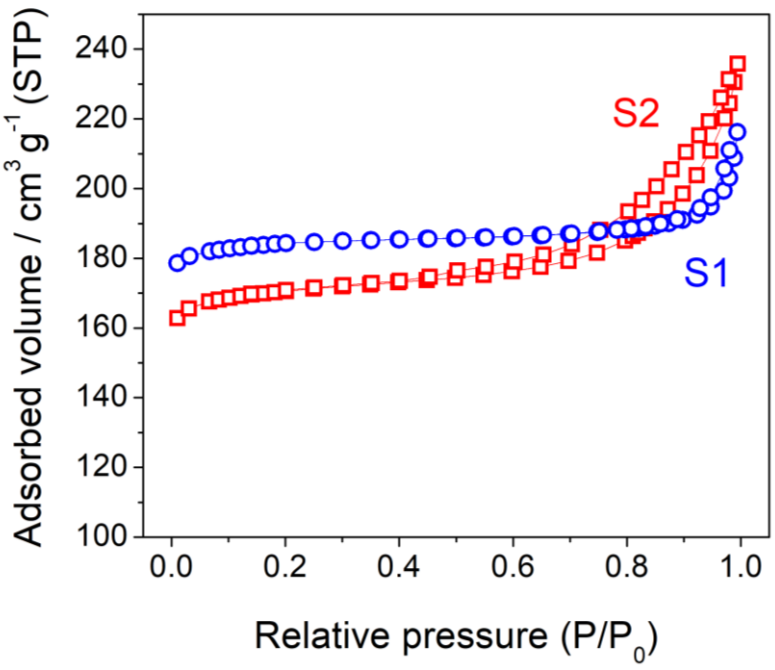

Figure 2. N_2 adsorption-desorption isotherms at 77 K for both SAPO-34 samples

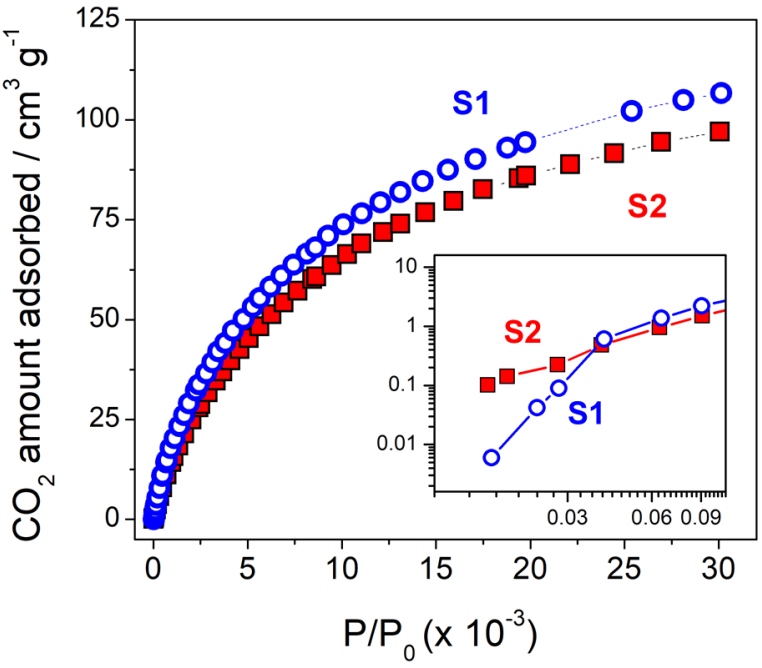

Figure 3. CO_2 adsorption isotherms at 25 ºC for both SAPO-34 samples

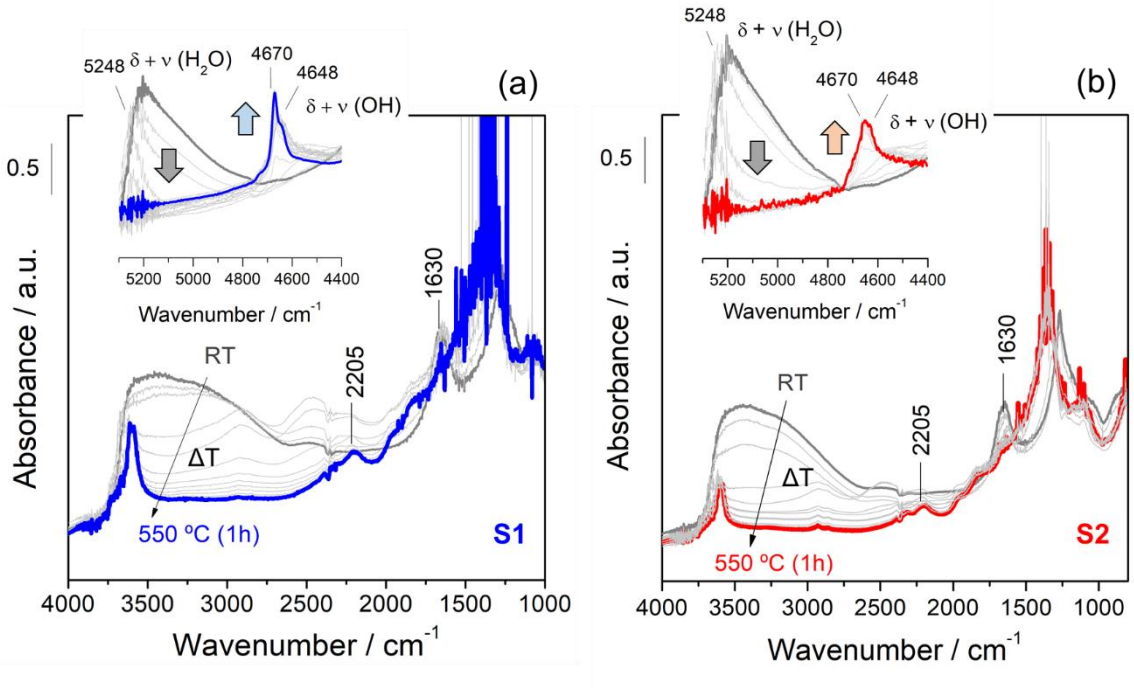

Figure 4. Evolution of the DRIFT spectra during the dehydration pretreatment from RT to 550 ºC fro 1 h under Ar flow on both SAPO-34 materials. Inset: DRIFT spectra in the combination bands region

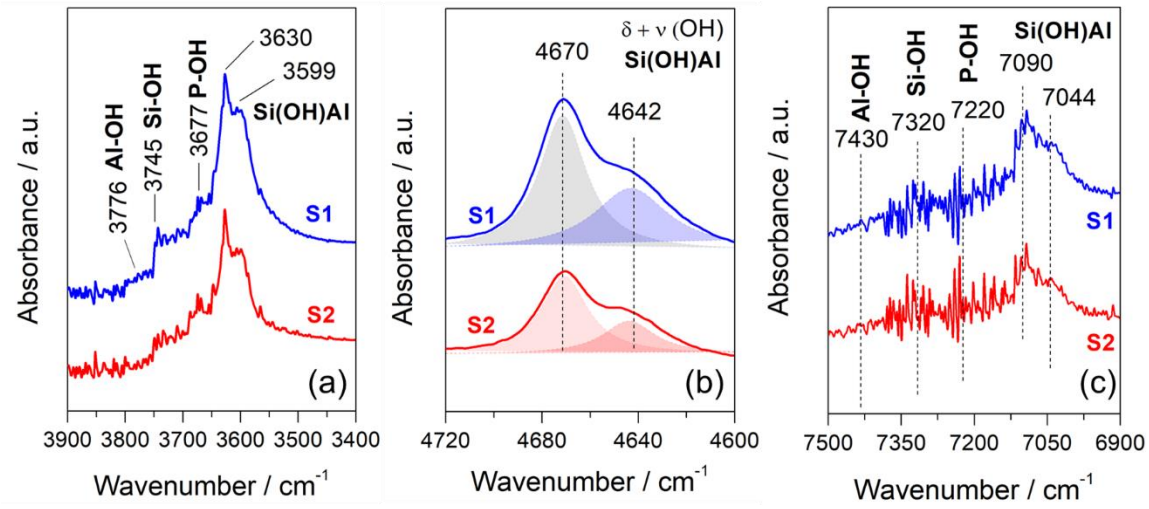

Figure 5. (a) DRIFT spectra in the fundamental stretching region of hydroxyls, (b) deconvolution of the DRIFT spectra in the 4800 – 4600 cm^{-1} combination bands region, and (c) DRIFT spectra in the first overtone region on the two SAPO-34 materials after dehydration pretreatment at 550 ºC for 1 h in Ar flow

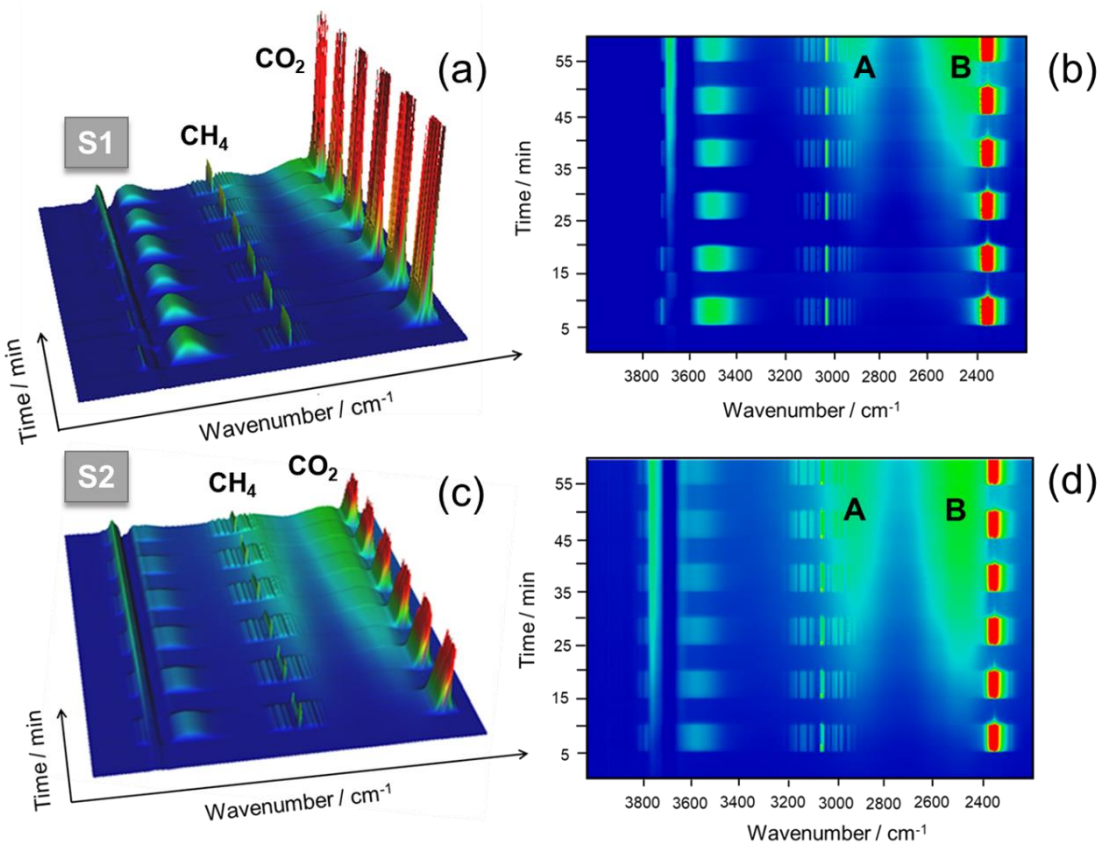

Figure 6. 3D evolution and 2D mapping representation of the IR spectra collected during the adsorption-desorption cycles at 25 ºC on both S1 (a-b) and S2 (c-d) SAPO-34 samples

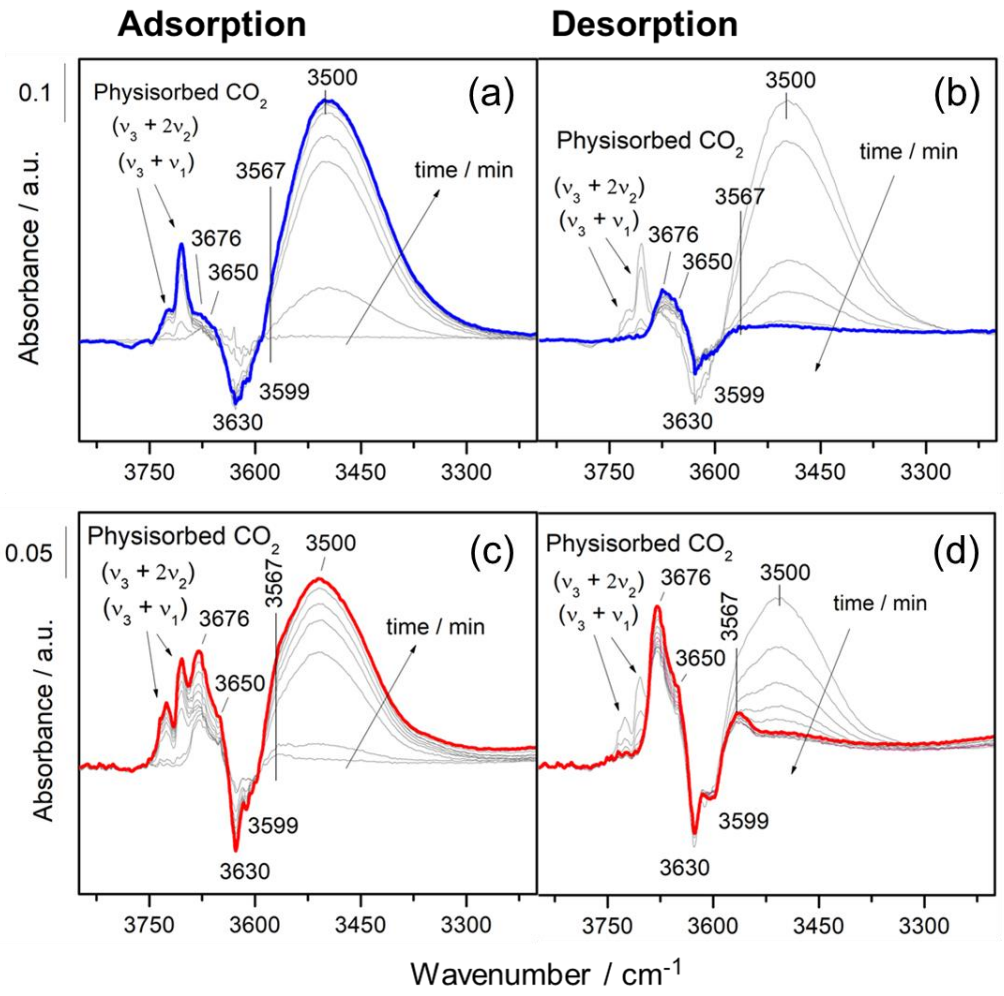

Figure 7. Representative evolution of DRIFT spectra in the fundamental stretching region of hydroxyls during the first cycle of adsorption/desorption at 25 ºC on both samples: (a) adsorption and (b) desorption on S1 SAPO-34; (c) adsorption and (d) desorption on S2 SAPO-34.

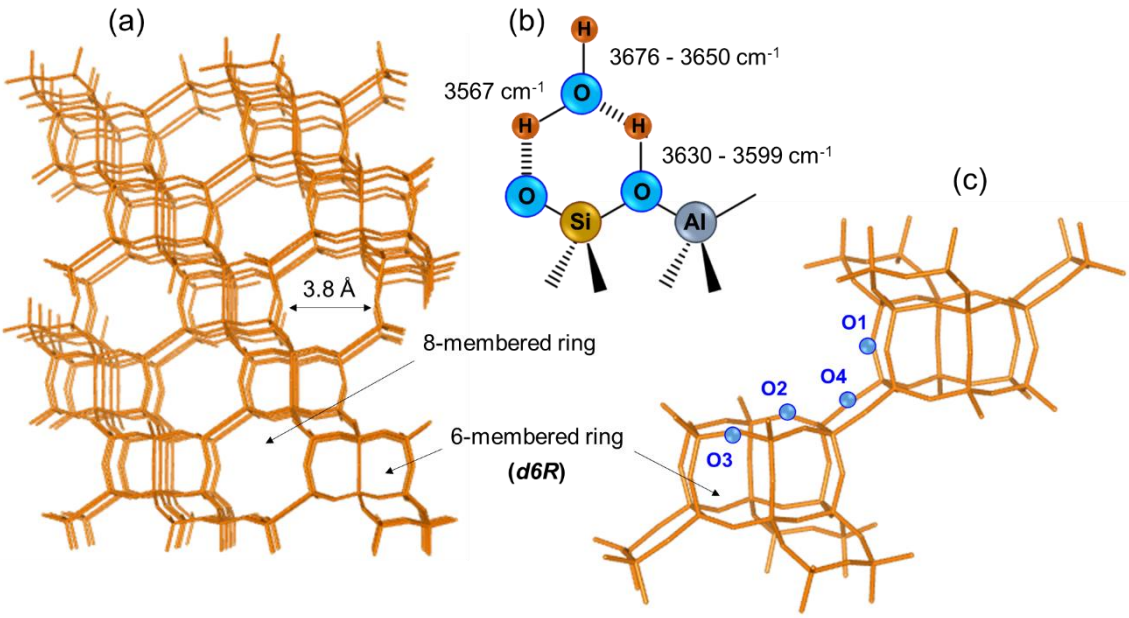

Figure 8. (a) Schematic representation of the chabazite (CHA) topology, (b) drawing scheme of the interaction of water with the Si(OH)Al acid sites and the associated stretching vibrational modes, and (c) unit cell of the CHA structure with the four different crystallographic positions of the oxygen into the framework

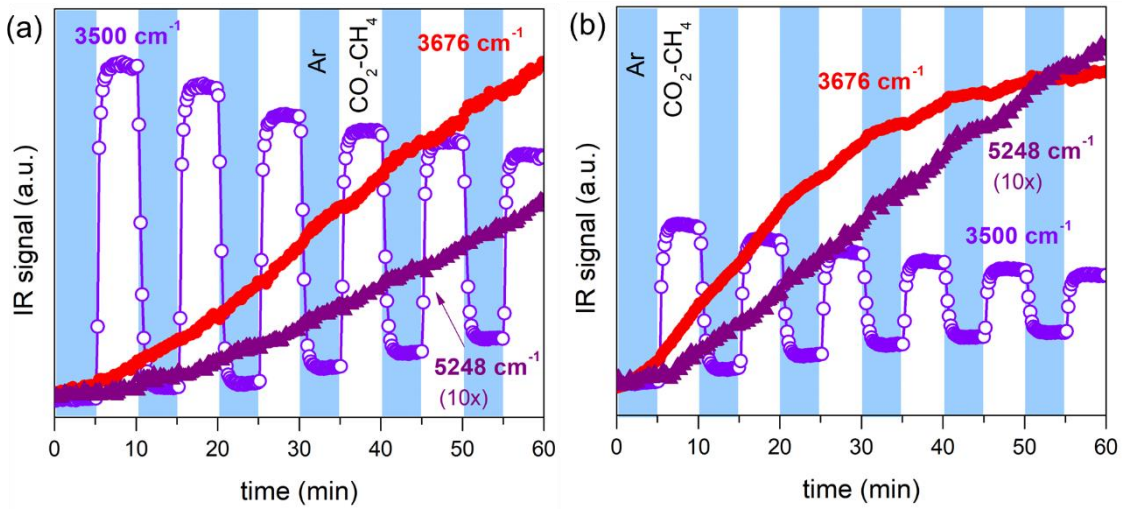

Figure 9. Evolution of selected IR peaks typical of physisorbed CO_2 (3500 cm^{-1}), adsorbed water at low coverage (3676 cm^{-1}) and molecular water occluded inside the cavities (5248 cm^{-1}) in both S1 (a) and S2 (b) SAPO-34 samples